Medical & Biological Engineering & Computing
https://doi.org/10.1007/s11517-023-02994-w

ORIGINAL ARTICLE

Improving signal-to-noise ratio by maximal convolution of longitudinal and transverse magnetization components in MRI: application to the breast cancer detection

Mansour Ashoor[1] · **Abdollah Khorshidi**[1]

Received: 28 July 2023 / Accepted: 7 December 2023

Abstract

Purpose The extraction of information from images provided by medical imaging systems may be employed to obtain the specific objectives in the various fields. The quantity of signal to noise ratio (SNR) plays a crucial role in displaying the image details. The higher the SNR value, the more the information is available.

Methods In this study, a new function has been formulated using the appropriate suggestions on convolutional combination of the longitudinal and transverse magnetization components related to the relaxation times of T1 and T2 in MRI, where by introducing the distinct index on the maximum value of this function, the new maps are constructed toward the best SNR. Proposed functions were analytically simulated using Matlab software and evaluated with respect to various relaxation times. This proposed method can be applied to any medical images. For instance, the T_1- and T_2-weighted images of the breast indicated in the reference [35] were selected for modelling and construction of the full width at x maximum (FWxM) map at the different values of x-parameter from 0.01 to 0.955 at 0.035 and 0.015 intervals. The range of x-parameter is between zero and one. To determine the maximum value of the derived SNR, these intervals have been first chosen arbitrarily. However, the smaller this interval, the more precise the value of the x-parameter at which the signal to noise is maximum.

Results The results showed that at an index value of $x = 0.325$, the new map of FWxM (0.325) will be constructed with a maximum derived SNR of 22.7 compared to the SNR values of T_1- and T_2-maps by 14.53 and 17.47, respectively.

Conclusion By convolving two orthogonal magnetization vectors, the qualified images with higher new SNR were created, which included the image with the best SNR. In other words, to optimize the adoption of MRI technique and enable the possibility of wider use, an optimal and cost-effective examination has been suggested. Our proposal aims to shorten the MRI examination to further reduce interpretation times while maintaining primary sensitivity.

Significance Our findings may help to quantitatively identify the primary sources of each type of solid and sequential cancer.

Keywords Convolution operator · Spin-spin relaxation time · Spin-lattice relaxation time · Breast cancer · MRI · Signal to noise ratio

Highlights
- New function of M(t) was introduced to increase SNR of any medical image.
- Longitudinal and transverse magnetized vectors convoluted and normalized by defining α^*.
- FWxM map was defined via full width in a fraction (x) of the maximum value of $M_{Normalized}$.
- The best SNR transpired at distinct x-parameter of 0.325 by 22.7.
- Obtained new maps can help quantify the early causes of breast cancer.

1 Introduction

Medical imaging systems that produce qualified images using the non/ionizing radiation can directly affect the diagnosis. MRI has been known as a powerful non-invasive tool in the medical field due to its unique properties. Two quantities that may show important information about the objects

✉ Abdollah Khorshidi
abkhorshidi@yahoo.com

Mansour Ashoor
ashoor_44@yahoo.com

[1] Radiation Applications Research School, Nuclear Science and Technology Research Institute, Tehran, Iran

Published online: 15 December 2023

in MRI are longitudinal (T_1) and transverse (T_2) relaxation times. A lot of the statistical and dynamical parameters can vary these times. For example, they may be varied in different situations by the geometric structure of the capillary bed [1–7].

T_1 is the irreversible evolution of a spin system toward thermal equilibrium with the orbital degrees of freedom of the medium in which the spins are embedded, named the lattice. This includes all observable spin variables such as longitudinal or transverse magnetizations, spin-spin energy or multiple-quantum coherences. It is only when the evolution is due to static spin-spin interactions, the spin-spin or transverse relaxation was considered [8]. The types of tissues and the others have a unique T_1-value that resolves those in the image. T_2 relaxation refers to the progressive dephasing of spinning dipoles resulting in a decrease in the magnetization in the transverse plane. It arises due to tissue-particular characteristics, primarily those that affect the rate of movement of protons, most of which are found in water molecules, and it also occurs in a varying local magnetic field when energy is transferred between dipoles aligned parallel and antiparallel to the external magnetic field and flipping each other in opposite directions. This rate of flipping or energy transfer between spins or dipoles increases as the frequency of the variation of the local magnetic field approaches the Larmor frequency. This is related to the rate of rotation and translation of the water molecule or neighboring dipoles. The dipole-dipole interaction also increases the strength of the local field which depends on the proximity of the neighboring dipoles. In pure water, T_2 is long, about 3–4 s, because water molecules move significantly faster than the Larmor frequency. The rapid movement causes T_1 and T_2 to be approximately equal in pure water. The analytical relationship between these relaxation times has not been fully understood yet. The combination of these times may create new maps containing more information for better diagnosis in the medical field, along with the good signal-to-noise ratio (SNR) that has been examined in this study. For instance, the images of the breast have been chosen here.

Recently, Yavuz and Eyupoglu [9] approached a prediction model based on anthropometric data and collecting parameters via routine blood analysis to classify patterns of transformed features through a non-iterative nature of neural network training on the recent Breast Cancer Coimbra Dataset (BCCD) with an average accuracy of 97% in an intra-class shuffling scheme. Since the MRI and mammography images can only be acquired preoperatively, the perspective changes during the operation compared to the images taken preoperatively. For example, mammography images are 2D images from two different orientations (cranio-caudal and medio-lateral-oblique) and are projected ad hoc in the physician's imagination during the operation [10]. The challenge always lies in the highly flexible breast tissue, the patient-specific breast shape and the connection of the breast to the chest wall. On the other hand, Liu et al. [11] presented a dynamic contrast-enhanced MRI method that utilizes dynamic and texture features to classify the breast lesions. Experimentally, they achieved a maximum accuracy of 0.73 and 0.86, respectively, for dynamic and texture features by 94% sensitivity. More importantly, feature selection may remove features that have little impact on classification, but there were still some limitations as their proposed method was not used for more accurate grading. Furthermore, Zadeh Shirazi et al. [12] proposed a computational intelligence model based on supervised and unsupervised learning methods via self-organizing map (SOM) and complex-valued neural network (CVNN), enabling reliable detection of breast cancer. They reported reaching 95% and 94% of disease and health ratios, respectively. Regardless of the improvement in imaging technology, accurate segmentation of the breast border and detection of tumors or even pectoral muscle are still challenging tasks for image processing algorithms. Moreover, Mustra et al. [13] investigated various segmentation techniques for detecting breast boundary based on thresholding, morphological operations, region growing, and active contours in which tumors were essentially not considered.

Hereupon, Ertas et al. [14] presented a volumetric segmentation technique which it is applicable to multi-center MRI to support computer-aided breast tissue analysis besides density assessment and lesion localization. They employed Bias-corrected fuzzy C-means clustering and morphological operators on T_1-weighted images without prior breast anatomy information. The breast–air boundary can be easily identified by looking for a large increase in the image intensity from the air side, provided that the background noise is low [15–17]. However, detection of the breast–chest wall boundary or tumor edges is a complicated issue due to coil-related intensity inhomogeneity artifacts and partial volume problems, especially in the presence of dense breast tissue connected to the chest wall muscles and liver tissue beneath chest wall muscles or in metastatic conditions [18, 19]. It should also be noted that a general problem for the segmentation community is that the ideal situation of T_1-weighted images without fat suppression is currently rarely encountered in routine clinical practice. Fat-suppressed sequences will pose difficulties for many of the algorithms so far presented in the literature to date, as there is no strong boundary between the fat of the breast and the chest wall or even between scattered solid tumors, and both appear hypo-intense on images. Nonetheless, it should be emphasized that any use of segmentation in a routine clinical context may require alterations in acquisition protocol that could lengthen the standard breast examination.

The breast cancer may be the involvement of dissimilar categories or amalgamation of invasive and in situ tumor.

These tumors have been characterized by the MR-mammography, which is a noninvasive method without energy deposit and standard safety [20–25]. The breast-MRI screening has the maximum sensitivity for recognition the tumor and is not limited by breast density [26]. On the other hand, due to greater availability and lower implementation costs, ultrasound scanning is more commonly utilized in complementary studies at this time. However, its cost-effectiveness is questionable as only a small excess yield of cancer was found [27]. Comparatively, MRI screening significantly is outperforming ultrasonography in progressive cancer yield (3–4 per 1000 vs. 15 per 1000) and takes a lower false-positive ratio compared to ultrasound method screening [28, 29] which it offers that MRI method might be the better adjunctive screening pathway for women with dense breasts.

Recently, Liu et al. [30] presented an MRI breast tumor detection method based on ultra-wideband microwave to extract representative features by 84% accuracy derived from Principal-Component-Analysis feature selection besides Gaussian Support-Vector-Machines through limited and distinct breast phantom structures. Since MR images have sparse representation in transformed domain by finite differences or cosine transform, Yin et al. [31] introduced a singular value threshold (SVT) method besides de-noising process to restore multi-slice MR images from k-space via inverse Fourier transform. They used compressive sampling to find sparse solutions of an underdetermined linear system in which reconstruction after transformation generates distinct artifacts and noise that degrade the quality of the breast image and decrease the SNR.

The quantity of signal to noise ratio (SNR) is a significant factor which influences the quality and performance of systems that transmit and/or process signals like data acquisition and imaging systems. A great SNR denotes that the image is clear and easy to recognize or deduce, while a low SNR denotes that the image has been degraded via noise and may be harshly recovered or recognized. The SNR may be enhanced through various approaches like signal strengthening, utilizing error correction techniques, noise level decreasing, and also unwanted noise filtering out. The more the SNR value, the better accessible on the information will have (https://en.wikipedia.org/wiki/Signal-to-noise_ratio) [32].

In this study, a new function using the appropriate suggestions on convolutional combination of the longitudinal and transverse magnetization components (vectors) related to the relaxation times in MRI is proposed in which by introducing the distinct index on the maximum value of this function, and then the new maps named FWxM-map are produced toward the best SNR.

2 Materials and methods

Variable orthogonal vectors with time such as longitudinal and transverse magnetization components are able to create a new vector with appropriate properties. Convolutional combination of them leads to an important mathematical function, which is addressed here.

2.1 Theory

One may consider the T_1 and T_2 relaxation times as macroscopic and microscopic aspects, respectively. However, each magnetic dipole exists in a microenvironment is unique to the tissue to where it belongs. In all tissues, there are tiny magnetic fields generated by the spinning hydrogen nuclei. As is known, the tip of the magnetization vector (**M**) moves in a helical manner on the surface of a sphere around the B_0 magnetic field, while the length of this vector remains constant. Resonance excitation may be considered at **(a)** in a rotating frame of reference, which rotates with the Larmor frequency ω_0 around the direction of the $\mathbf{B_0}$ field, the magnetization **M** precesses with the frequency ω_1 around the stationary $\mathbf{B_1}$ field, and **(b)** in the stationary frame this simple rotation is superimposed by the markedly faster rotation around the z-axis. Therefore, the tip of the vector **M** moves in a helical manner on the surface of a sphere as shown in Figure 1.

The exponential relaxation of the longitudinal and transverse magnetization components after excitation of the spin system by a 90° pulse is shown in Figure 2, and gives a simple interpretation of these relaxation times. In other words, after excitation by a 90° pulse, the longitudinal magnetization M_z relaxes toward the equilibrium magnetization $M_z = M_0$, and the transverse magnetization toward $M_{xy} = 0$. The temporal evolution is defined by the relaxation times T_1 and T_2, respectively. The T_1 gives the time required for the longitudinal magnetization after a 90° pulse to grow again to 63% of its equilibrium value M_0, and the T_2 gives the time required for the transverse magnetization after a 90° pulse do drop to 37% of its original magnitude.

Mathematically, a convolution is defined as the integral over the entire space of a function in x multiplied by another function in $u-x$. The integration is taken over the variable x, characteristically from minus infinity to plus infinity in all dimensions. Therefore, the convolution is a function of a new variable u, as presented in Eq. (1).

$$C(u) = f(x) \circledast g(x) = \int_{-\infty}^{+\infty} f(x) \times g(u - x)dx \tag{1}$$

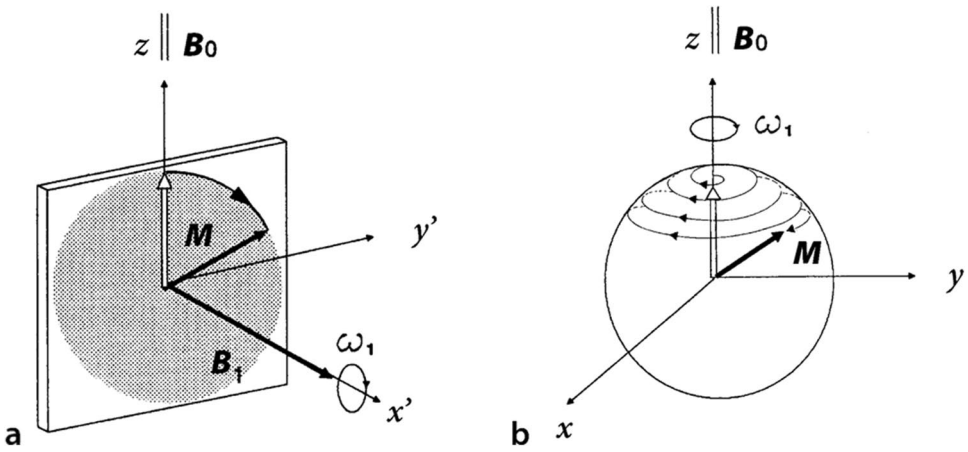

Fig. 1 Resonance excitation a in a rotating frame of reference and b in the stationary frame

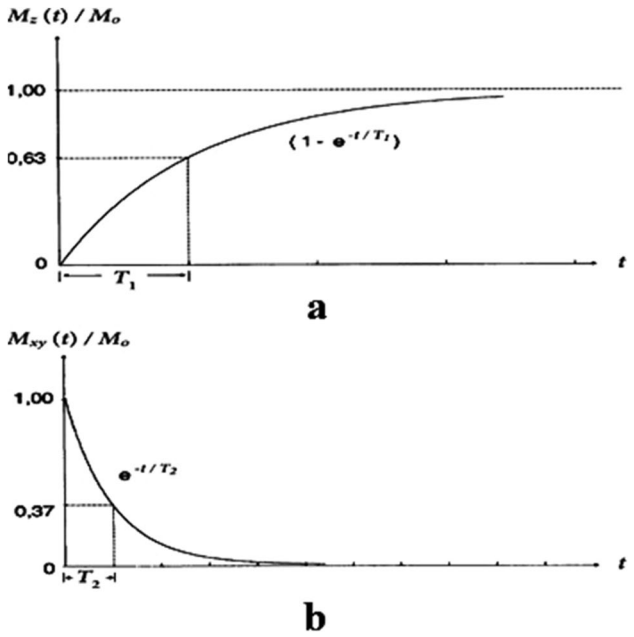

Fig. 2 Relaxation of the a longitudinal and b transverse magnetization

If one of the functions is unimodal, as shown in Figure 3, the other function is shifted through a vector equivalent to the peak position and also smeared by a quantity that depends on the sharpness of the peak (https://www-structmed.cimr.cam.ac.uk/Course/Convolution/convolution.html). The features of convolution technique on the functions of spin-lattice (T_1) and spin-spin (T_2) relaxation times or the convolution of two orthogonal magnetization vectors are used to achieve the qualified images with the good SNR. The T_1 and/or T_2-weighted images in MRI are used intensively to recognize the abnormal tissues and tumors.

The amounts of magnetized vectors of longitudinal M_z (t) and transverse M_{xy} (t) with respect to these relaxation times are formulated as follows:

$$\frac{M_{xy}(t)}{M_0} = e^{-\frac{t}{T_2}}, \text{and} \frac{M_z(t)}{M_0} = 1 - e^{-\frac{t}{T_1}} \tag{2}$$

To extract some of information from the T_1- and T_2-maps together, a new function named M(t) has been suggested between them as follows:

$$\mathrm{M(t)} = \frac{\mathrm{M_{xy}(t)}}{\mathrm{M_0}} \circledast \frac{\mathrm{M_z(t)}}{\mathrm{M_0}} \tag{3}$$

where $\circledast$ indicates the convolution operator. The M(t) function always has a maximum value (peak). The value of this peak after normalization of M(t) denoted as $\max\left(\mathrm{M_{Normalized}}(\alpha)\right)$. Using the $\mathrm{M_{Normalized}}$ (t) function in which interactions between these relaxation times are included via convolution aspect, the values of α^* are computed from the following function:

$$\alpha^* = \mathrm{M^{-1}_{Normalized}}\{\mathrm{x} \times [\max\left(\mathrm{M_{Normalized}}(\alpha)\right)]\} \tag{4}$$

where x is the parameter on range from zero to one. Finally, the new index as FWxM defined as full width in a fraction (x) of the maximum value of the $\mathrm{M_{Normalized}}$ function ($\max\left(\mathrm{M_{Normalized}}(\alpha)\right)$) will be computed for creating the new maps with the SNR better than the T_1 or T_2 one named improved SNR, as follows:

$$\mathrm{FWxM} = \alpha^*_{\max} - \alpha^*_{\min} \tag{5}$$

Furthermore, the best SNR transpires at the distinct x-parameter. The proposed function was simulated using Matlab (R2016a, MathWorks Inc., MA) software, and evaluated in terms of various relaxation times and the different amounts

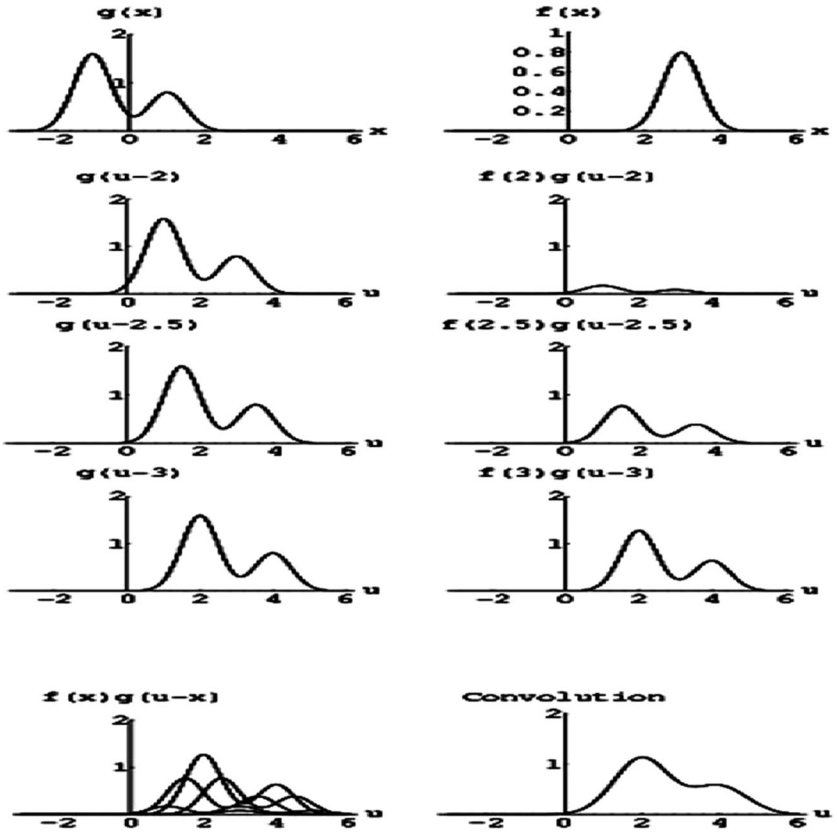

Fig. 3 Illustration of convolutional method

of x-parameter in order to obtain the new maps named the FWxM-map.

3 Results

The proposed theory via orthogonal M_{xy} and M_z vectors convolution was simulated at distinct amounts of T_1 and T_2, for instance 60 and 10 ms, respectively, as shown in Figure 4. The exponential curves of the corresponding magnetization vectors were plotted numerically for these arbitrary T1 and T2 amounts. Then, their convolutions as a new function was also plotted and finally the FWxM for $x = 0.5$, which corresponds to 31 ms, was determined.

The T_1- and T_2-weighted images of the abnormal breast have been considered for investigation under our proposed theory. The T_1- and T_2-weighted images of the breast from the reference [33] were chosen for simulation and production of the FWxM-map at the various values of x-parameter from 0.01 to 0.955 at 0.035 and 0.015 intervals, respectively, as shown in Figs. 5 and 6. The input images have SNR values by 14.53 and 17.47, respectively, for T1 and T2 images. Subsequently, the maximum SNR values were 22.70 and 22.69 at x of 0.325 and 0.330, correspondingly.

Here, to show more details and cause of this event, the amounts of SNR at different x-parameters for the new maps are calculated [34]. The SNR has been improved at the values of x from 0.185 to 0.430, which is maximized at value of 0.325, as shown in Figure 7. The maximum-SNR of 22.7 was at the distinct index of $x = 0.325$. Figure 8 shows the generation of more images at the maximum range of Figure 7 by decreasing the x interval.

The SNR is increased with the increasing x-parameter indicated in Eq. (4) toward a maximum value where the best SNR is denoted at the distinct x-parameter, and then the SNR is decreased.

This behavior is due to the convolution of two function as integrator and differentiator, resulting to the maximum point. The x-parameter characterizes the interactions between the relaxation times in point of view the quantum aspects, which should be evaluated more in the future. The increase of the signal at a distinct x-parameter has proved that most information from the subjects can be transpired via an alternative pathway that might have been potentially sufficient.

According to Figure 9, we fitted the output SNR with a function that uses a fifth degree polynomial here and is shown in Eq. (6). Here, the SNR as a function of the x-parameter values may be formulated as follows,

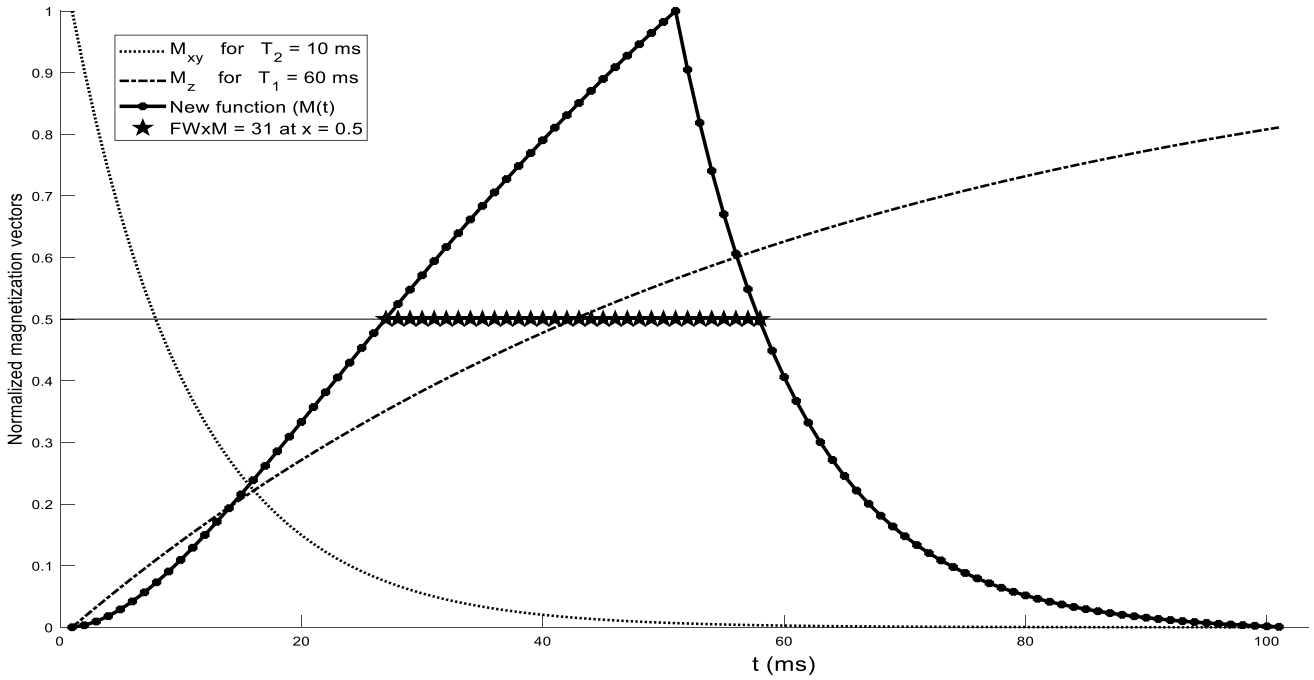

Fig. 4 Distinct numerical illustration of M_{xy} and M_z vectors and their convolution besides derived FWxM at $x = 0.5$

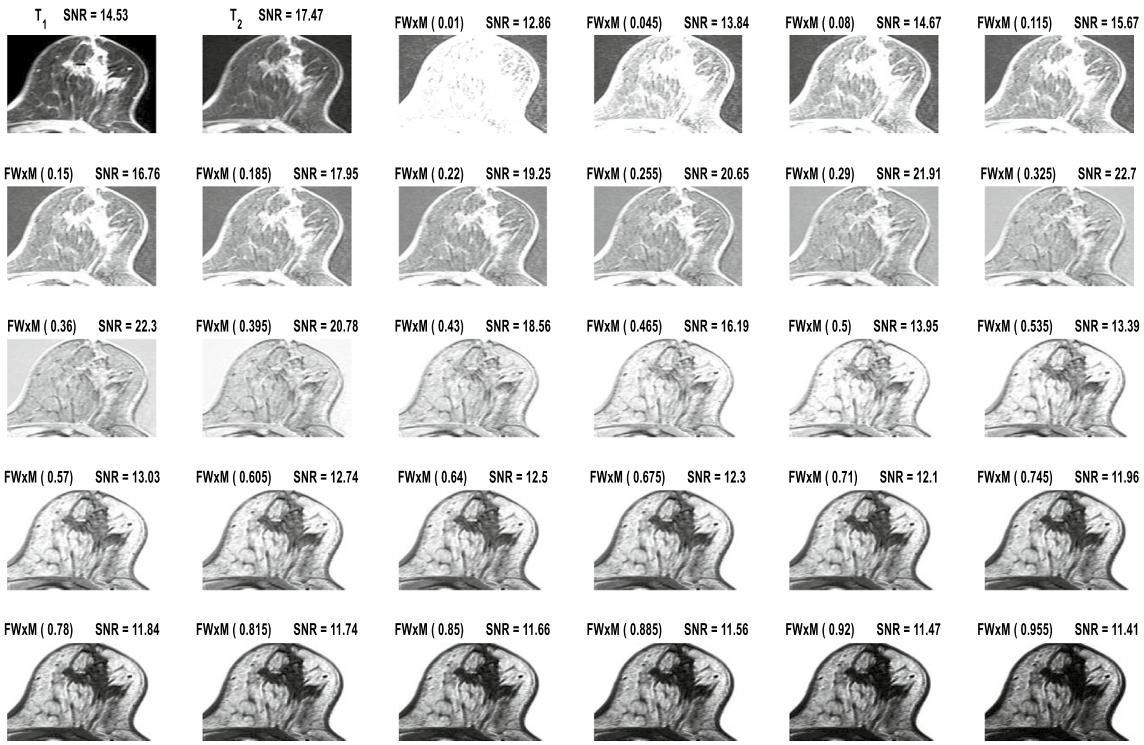

Fig. 5 The FWxM-map produced based on the proposed theory at the various indices 0.01 through 0.955 at 0.035 intervals [33]

$$\mathrm{SNR} = \frac{p_1 x^5 + p_2 x^4 + p_3 x^3 + p_4 x^2 + p_5 x + p_6}{x^5 + q_1 x^4 + q_2 x^3 + q_3 x^2 + q_4 x + q_5} \tag{6}$$

where x is normalized by mean 0.5 and standard deviation (STD) of 0.298. Coefficients of p_1, p_2, p_3, p_4, p_5, p_6, q_1, q_2, q_3, q_4, and q_5 were as 11.85, 32.86, 27.88,

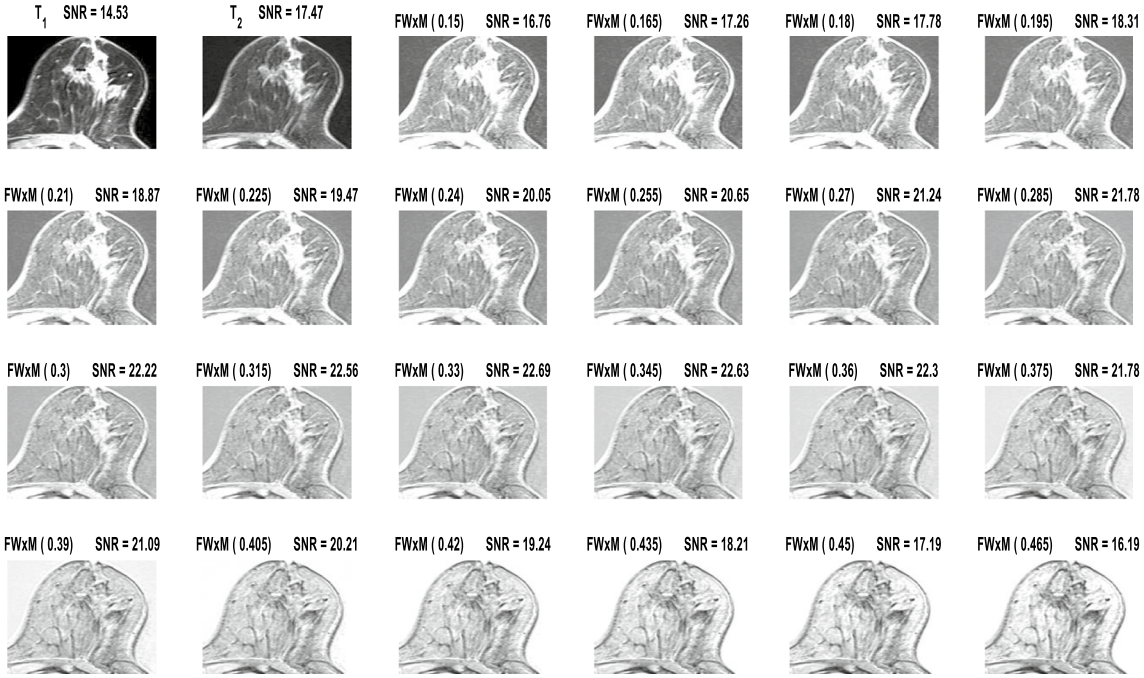

Fig. 6 The FWxM-map produced based on the proposed theory at the various indices 0.15 through 0.465 at 0.015 intervals [33]

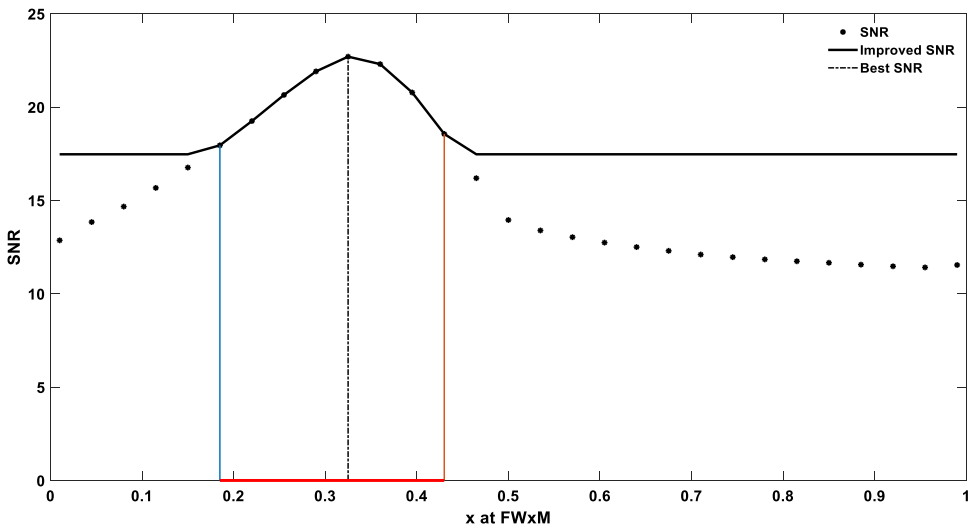

Fig. 7 The calculated amounts of SNR at the different values of x-parameter for the FWxM-map. The SNR has been improved at the values of x from 0.185 to 0.430 (red segment). The maximum-SNR of 22.7 was at the distinct index of 0.325

18.03, 0.8245, 0.5851, 2.995, 2.527, 1.175, 0.09485, and 0.04176, respectively with 95% confidence bounds, as shown in Fig. 9. Now, any x we assign to this function can get the SNR even if it is not mentioned in Fig. 5, since here, we have continuously extracted the fitting function. The sum of squares derived from error (SSE), R-square, adjusted R-square, and root mean squared error (RMSE) values were 0.07305, 0.9998, 0.9997, and 0.637, respectively, in which RMSE is the standard deviation of the residuals, so-called prediction errors. The residuals are a measure of how far data points are from the regression line. In other instances, RMSE is a measure of the degree of dispersion of these residuals. The amount of error is also shown in the bottom diagram of Fig. 9 for each point in order and proportion, with some points having positive error and some points having negative error. Those constant values may indicate some features of the image due to the physiological parameters and pathphysiologic conditions, which will be investigated probably by the researchers in the future study.

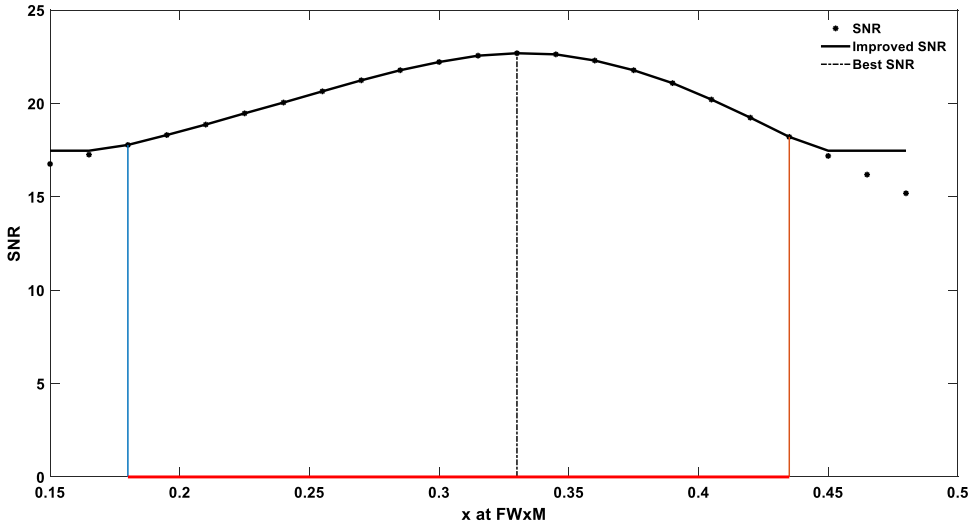

Fig. 8 Generation of more images at the maximum range of Fig. 7 by reducing the x interval

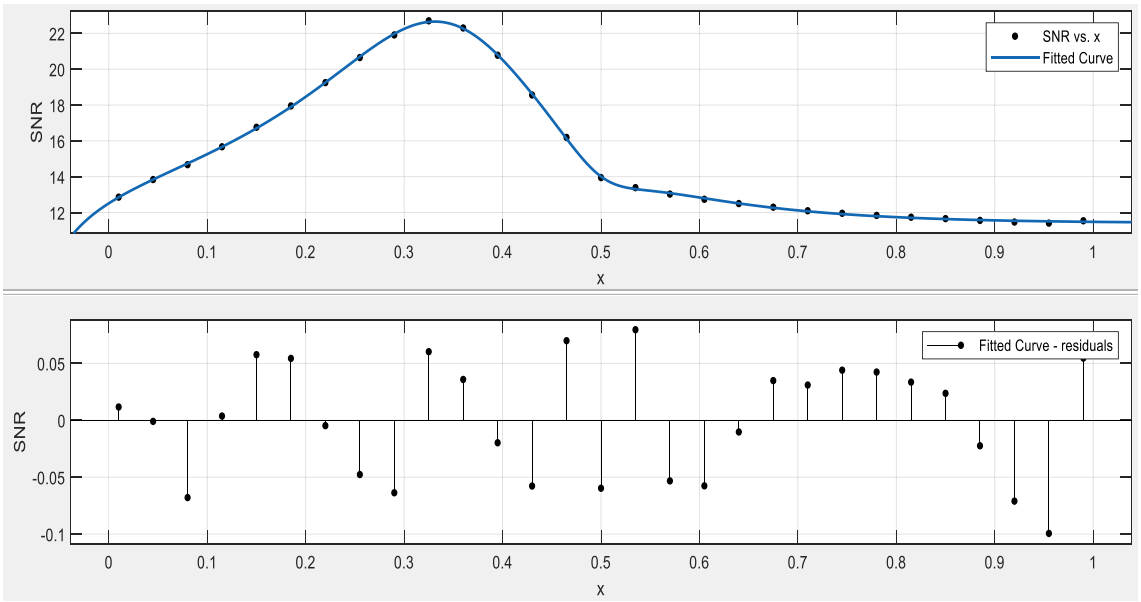

Fig. 9 The SNR as a function of the x-parameter values (top) along with the residual values (bottom)

4 Discussion

In this study, an appropriate theory was introduced to obtain the new maps by the hybrid combination of the transverse and longitudinal relaxation times to improve the SNR and find the best SNR. In other words, a novel function of relaxation times in MR imaging was evaluated using the convolution operator. The creation of the new maps can help prevent further damage form imaging problems and also treatment issues, and quantitatively reveal the preliminary causes of breast cancer. Also, our finding may help grade the different tissues and estimate the duration of the healing trends by evaluating the maps extracted from the proposed theory.

In our proposed theory, according to Eq. (3), when two magnetization vectors M_{xy} and M_z are convolved, their special effects are introduced with a special function, which we called M(t). Furthermore, according to Figure 2, M_z increases exponentially, but M_{xy} decreases exponentially. As a result, with two exponential functions, one ascending and the other descending, it concludes a curve that peaks and then descends like a pulse or parabola. The resulting function was then normalized, that is, the maximum value equal to one was considered. Therefore, the convolved function is

maximized at some points of this curve. Then, this maximum value was examined between $x = 0$ and 1 with arbitrary intervals, here 0.035 and 0.015, where the shorter interval generates higher accuracy but longer program execution time. Afterwards, the parabolic curve was compared with its maximum function, which generates the new points that intersect each other as minimum and maximum alpha, and we call their difference FWxM. For example, as the studied intervals decrease from 0.015 to 0.010 (Figs. 5 and 6), more images will be constructed over a longer period of time, which can show more structural details to the physicist.

However, according to Figs. 5 and 6, as x increases, the SNR value decreases for the reason shown in Figs. 7 and 8, that is, according to Eq. (3), M(t) has a certain maximum and will therefore have a certain SNR. According to Eq. (4), the normalized M occurs at a certain alpha whose maximum is equal to one, and then it is multiplied by the value of x (that is, for example 0.9 or 0.1) and then we inverse the result to get alpha-star. As a result, so far we have two alpha-star values, maximum and minimum, located on either side of the peak of the paragon curve and defined by their difference as FWxM, and this proposed function will give different images in different x. Now we need to assign the different x's a number between zero and one, which is arbitrary since our goal is to achieve the highest SNR. According to Figs. 5 and 6, two T_1 and T_2 images with a specific SNR were obtained from reference [33], and the derived images were processed for different x. For example, in Figure 5, with these two specific primary images T_1 and T_2 and intervals of 0.035, the highest SNR was obtained at $x = 0.325$.

The presented method can be applied to all images acquired from T_1 and T_2 relaxation times, such as brain images. In this study, breast images were selected as examples from reference [33] due to the global spread of breast cancer and also its complex and unique structures. Normally, the various T_2 images can be obtained from different echo time (TE) and repetition time (TR), and as a result, different images can be acquired, which means that these times should be applied in practice, which increases the time of using the device. But in our proposed theory, with the convolution of two relaxation times of T_1 and T_2, it is possible to estimate several and various images with dissimilar SNR, and finally the computed SNR derived from our theory were greater than the primary SNR from the original T_1 and T_2 images.

According to Figure 7, the calculated SNR points have been obtained based on the proposed method and in the range of $0 < x < 1$, i.e., exactly between less than 0.2 and more than 0.4, and their value was greater than the primary SNR = 17.47 of the input T_2 image of Fig. 5. So, this limited range gives the correct result according to the proposed theory and the rest of the range between 0 and 1 is no longer useful for our detailed study. According to Fig. 8 and in this selected interval, the number of derived images has now been increased, which means that the x-intervals have been reduced and finally 18 new output images have been generated with their specific FWxM in this limited range.

Practically, in a T_2 image, when the echo time or repetition time changes, one of these calculated images may be obtained and therefore the image acquisition time can be said to be controllable or reduced. This does not mean that the image acquisition time during MRI scanning is directly shortened, but that according to the proposed theory, an image with a higher derived SNR can be obtained, which is the same scanning time as the initial image acquisition. Congruently, it can be said that in experimental imaging, the scanning time is reduced because a higher new SNR value is estimated from the convolution process.

Among the existing and routinely practiced methods for early breast cancer detection, MRI has the highest sensitivity. Recently, Kuhl et al. conducted a study over an 8-year period and reported a 95% confidence interval of 96.5–97.6% for specificity with a positive predictive value of 35.7% in diagnosing high-grade breast tumors as small as 8 mm. A chief limitation of clinical MRI is its wide range of specificity by 37% to 97%, which manifests itself in errors in distinguishing between malignant breast tumors and benign lesions [35]. Nonetheless, false-positive MRI results in high-risk lesions are significantly different from the false-positive results on radiographs associated with low-risk lesions [36].

Image contrast based on tissue T_1 and T_2 are common MRI sequences that exploit the differences in relaxation times of protons within the examined tissue. T_1 provides a longitudinal relaxation time while T_2 provides a transverse relaxation time for a series of protons. By leveraging the different T_1 and T_2 relaxation characteristics of different tissues, static MRI provides superior structural contrast between adipose and fibro-glandular tissue and remains a mainstay for risk analysis, tumor detection and treatment monitoring. Dynamic MRI methods go one step further and clarify the functional properties of malignant tumors. Dynamic contrast-enhanced (DCE) MRI detects T_1 variations in tissue over time immediately following bolus administration of a gadolinium-based contrast agent. The hyper-vascularity of breast tumors leads to altered uptake and washout ratios, and the unique time-intensity curve can separate malignant from benign tumors. However, recent concerns about persistent gadolinium accumulation and toxicity have affected patient compliance with methods requiring a gadolinium-based contrast agent, including DCE-MRI, and research efforts have been improved to develop alternative, noninvasive approaches. A major contender is diffusion-weighted imaging (DWI), which has already proven to be a valuable complement to DCE by improving combined sensitivity. DWI can elucidate tissue properties based on the Brownian motion of water. Since the diffusivity outside and

inside cells is different, the pattern of tissue morphology can be determined based on the restriction of movement of water molecules in densely packed cells [37]. Innovative procedures such as MRS and chemical exchange saturation transfer may shed light on the underlying chemical composition, provide snapshots of tissue metabolism, and characterize microstructural heterogeneity. Besides, non-compartmentalized, non-Gaussian diffusion models have the potential to derive micron-scale diffusion metrics that can reflect tumor heterogeneity and microstructural dimensions.

Here, in our study, the features of the convolution technique on the performance of spin-spin (T_2) and spin-lattice (T_1) relaxation times were used in breast cancer research to demonstrate the ability of better tumor discoveries.

Production of new maps with the best SNR can also contribute to better diagnosis and treatment. The qualified images with improved SNR were produced based on the proposed theory in which the convolution aspect plays a key role. The new index at the different values is able to obtain the different images with the different SNR values. The best SNR was obtained at the distinct index.

The x-parameter plays a key role to obtain the qualified images. This parameter can vary in the range between zero to one, which we need to determine at what value of x-parameter the SNR value is higher than that of the T_1- and T_2-weighted MR-images, leading the best SNR.

For example, to examine the theory, the breast images were selected from the reference [33]. We have evaluated the different values of x-parameter at intervals of 0.035 and 0.015 to obtain the maximum SNR. To achieve higher accuracy, this interval can be reduced to lower values, but the calculation time will increase.

As known, one of the most common categories of cancer in women is the breast cancer, that may be recognized on medical images. Evaluation of breast cancer at all the stages is very important in the medical field in which the treatment planning as well as prediction of its growth rate should be considered. The quantitative assessment of may be addressed via introducing our theory along with the appropriate suggestions in which the new images named FWxM-map along with the good SNR are produced. The SNR has been improved at the values of x from 0.185 to 0.430. The maximum-SNR of 22.7 was at the distinct index of 0.325, which is higher than that of the T_1 and T_2 maps. These maps may help to improve the better diagnosis on the breast cancer.

In any imaging system, as the SNR increases, the sensitivity also increases somehow. Here, the SNR, derived from a mathematical formula, was raised according to the proposed theory. It should be noted that the sensitivity of the device is not comparable to the proposed theory, because T_1 and T_2 imaging have been performed and abandoned with a specific sensitivity of the device, and we have nothing to do with it in the proposed theory. Briefly, two perpendicular curves (M_z is an ascending exponential function and M_{xy} is a descending exponential function) was convolved and a curve was extracted, the result of which is a parabolic curve with a peak. By convolution, the spin-spin and spin-lattice quantum energies are integrated simultaneously, so it is not possible to quantumly represent their exact effects on providing sensitivity. However, according to the proposed function, it can be seen that the maximum SNR can be achieved at a certain *x*. Furthermore, it should be noted that if another image is tested with this proposed theory, the derived maximum SNR value will definitely occur at a different x than 0.325 or 0.330 because T_1 and T_2 have different input amounts, and the results will be different for each input image by their convolution. Certainly, this theory will generate different results for other images such as brain or even other breasts. This process is important for physicists because the details of the image are important to better diagnose the tumor within the interwoven structures of the breast. Therefore, categorizing the tumor within a complex structure made up of different tissues with different densities can help the physicists make a better diagnosis.

The comprehensive symptom of the breast cancer is a new mass or a fresh lump, which the positron-emitting radionuclides can be applied to treat the breast. However, the geometrical structure of this mass should first be estimated. The dynamical maps derived from the projected theory may help accurately represent these structures. Various imaging tests can be performed for a variety of reasons, including to find out whether a suspicious area may be cancerous, to see how far the cancer cells have been dispersed, and to regulate whether the treatment pathway is working [38–41]. In addition, the images with the higher SNR can display the smaller lesions according to our theory.

Furthermore, there are many forms of breast cancer because it can occur in a specific region of the breast, like the lobules, the milk ducts, or the tissues between them. The nature of breast cancer is distinguished via distinct cells affected. Established upon the cell lineage involved, breast cancers can be categorized into two general groups: sarcomas and carcinomas. Sarcomas are a much rarer form of breast cancer by $< 1\%$ of primary breast cancers, and originate from the stromal elements, that comprise blood vessel cells and myofibroblasts. Carcinomas are breast cancers that originate from the epithelial element of the breast, which is made up of the cells that ceil the lobules and terminal ducts accountable for milk production. These categorizes are not always sufficient groups because in some cases a single breast tumor may be an amalgamation of diverse cell forms [42, 43]. Here in our study, the acquired new map with the best SNR may recognize these groups toward better diagnosis.

Uncharacteristic epithelial hyperplasia relates to a variety of proliferative epithelial lesions that are not obligatory

precursors to malignancy and also they are biological indicators of future increased risk of the breast cancer growth. Some women with uncommon epithelial hyperplasia like atypical lobular hyperplasia (ALH), atypical ductal hyperplasia (ADH), and lobular carcinoma in situ (LCIS) have a relative risk of breast cancer three to ten times greater than the general population [44]. While these women are presently categorized into the intermediate risk group according to the ACS-2007 strategies by 15%–20% lifetime risk (LTR) [45], recent data with long-term follow-up specify that these populations have an LTR higher than 20% that is more consistent with the high-risk categorization for which annual MR imaging would be suggested. This risk probably may be characterized with good SNR originated from the values of x-parameter in the FWxM-maps.

The excess cancer yield is highest with dominant MR imaging examinations and reduces with subsequent rounds of interim examinations because cancers that have gone undetected by routine sonography or mammography are first detected [28, 46]. Especially in mild node-negative invasive breast cancer, the sensitivity of MRI technology exceeds that of mammography [47, 48]. For instance, in a large randomized study available in the Lancet journal in 2019, that examined four rounds of screening in 1,355 women, MRI technique not only discovered more breast cancer cases than mammography (40 vs. 15 breast cancer cases, $p = 0.0017$), but also rarer and smaller node-positive cancers with mean size of 9 mm vs. 17 mm by $p = 0.010$ (11% vs. 63%, $p = 0.014$), leading to an important shift in tumor stage on MRI-screening group and signifying a potential for enhanced survival [40]. In addition, a divergent tendency was observed, in which the MRI technique more favorably detects invasive and major in situ disease, in contrast to mammography, which more favorably detects in situ and minor invasive disease [50], which highlights the intrinsic dissimilarities between anatomical and functional representation of the breast cancer. Although no direct appraisal of the MRI-specific conclusion on long-term survival in breast cancer is available, there are consistent data demonstrating a substantial enhancement in at least short-term survival (10 years) in high-risk women undergoing MRI technique compared to those who do not do this, since a more aggressive disease will be detected earlier [48, 49]. Furthermore, it has been assumed that the complementary MRI technique besides multi-round mammography reduces the incidence of interval cancer by up to 50% via detecting tumors with poorer prognostic properties and lower survival results, and thus should improve mortality [48–52].

Despite potential advantages of MR imaging, there are obstacles to broader use, mainly due to cost-effectiveness and limited availability. The MRI procedure via enhanced dynamic contrast is currently subject to certain technical constraints (slice thickness ≤ 3 mm, in-plane pixels ≤ 1 mm), and standard protocols include T_1- and T_2-weighted pre-contrast and three post-contrast sequences to construct a kinetic enhancement curve. As a result, a generic exam recording takes an average of 20 to 30 min per exam. Both the limited access to MRI machines and the long scan time are currently limiting the wider application of MRI technique. Also, the need for intravenous administration of contrast media and longer examination times are less tolerated at the patient level. Besides, the actual cost of the test may be high. When accounting for quality-adjusted life years gained in very high-risk women such as BRCA mutation carriers, MRI screening has been shown to be cost-effective, but it may be less cost-effective in non-BRCA women [53–55]. Nonetheless, there is evidence that MRI screening, when used routinely, has the potential over time to become more cost-effective than mammography, particularly as screening costs decrease [56].

To obtain the more images in which various information is included, one may change the values of time of echo, repetition time, and the others on the pulse sequences in MRI, but we created the qualified images with high SNR using the convolution of two orthogonal magnetization vectors with less time. In other words, in order to optimize the acceptance of MRI technique and to enable a broader usage, a suggestively optimized and more cost-effective examination is therefore necessary. Hence, current attempts are aimed at shortening the MRI examination to further reduce interpretation times while preserving primary sensitivity. Therefore, the obtained new map at the various indices with improved SNR based on our theory may more precisely display the spread of cancer breast at the early stages along with the amounts of the mass.

As is known, a hard mass with asymmetrical borders is painlessly more cancerous and can be easily tenderized or fractured. Other possible disturbances in breast cancer include pain in the breast tissue or nipple, swelling disorder, irritation or pitting of the skin, nipple or skin thickening, redness, scaling, and nipple discharge and retraction [57]. The mammary glands are made up of enormous chains of lobed ducts lined with epithelium that can secrete milk. These ducts feed into larger milk transport ducts that come together at the nipple. Evidently, these glandular structures are lodged in backing fatty tissue and the breast is divided into lobules through connective tissue. Consequently, the proposed FWxM function and its derived maps are able to accurately discern these structures at different stages with good correlation and more detail representation because of the best SNR.

As T1 and T2 change, the resulting convolution function also changes the shape of the extracted curves. This can be more investigated through the turning points of the

curve, the type of maxima, the integral or area under the curve, and the slope lines or the second derivative of the curves, which can categorize the tumor growth differently and specifically. For future work, these features can also be categorized for different lesions and linked to tumor grading.

5 Conclusions

The novel proposed technique is capable of obtaining more high SNR images in which we have only used the T_1- and T_2-weigthed MR-images with low SNR. Therefore, the acquisition time to interpret more qualified images will reduce. Our proposal aims to shorten MRI examination to further reduce interpretation times while maintaining the primary sensitivity to reach the qualified images with a higher SNR than the T_1- and T_2-weighted MR-images. This topic has been carried out by convolution of two orthogonal magnetization vectors. Characterizing or grading the tumor in any type of image, even non-breast tumors, using this mixed method of convolution and the maximum *x* interval results in different values of FWxM to obtain the best computed SNR and provide the derived image with more details. Categorization of convolution function originated from the longitudinal and transverse magnetization components may be used to grade tumors and lesions in the body organs, which may be studied in the future. In addition to that, the quality of medical images and the increase in signal-to-noise ratio can be evaluated using the contrast-to-noise ratio (CNR) parameter in future studies.

Author contribution AK: conceptualization, data curation, formal analysis, investigation, methodology, software, supervision, validation, visualization, writing—original draft and revising

MA: conceptualization, data curation, investigation, methodology, software, supervision, validation, writing—original draft

Data availability This manuscript has no associated data. All data required to support the results and conclusions of the study have been provided here with the submission. For each image that was taken from a reference, the name of that reference was also mentioned next to it or within the text.

Declarations

Ethics approval and consent to participate Not applicable

Human participants and/or animals No participation: "This article does not contain any studies with human participants or animals performed by any of the authors."

Consent for publication Not applicable

Conflict of interest The authors declare no competing interests.

References

1. Van Dijke CF, Brasch RC, Roberts TPL, Weidner N, Mathur A, Shames DM, Mann JS, Demsar F, Lang P, Schwickert HC (1996) Mammary carcinoma model: correlation of macromolecular contrast-enhanced MR imaging characterizations of tumor microvasculature and histologic capillary density. Radiology 198:813–818
2. Dennie J, Mandeville JB, Boxerman JL, Packard SD, Rosen BR, Weisskoff RM (1998) NMR imaging of changes in vascular morphology due to tumor angiogenesis. Magn Reson Med 40:793–799
3. Bihan DL (1995) Diffusion and perfusion magnetic resonance imaging. Raven Press, Ltd New York, chapter 15:270–274
4. Ashoor M, Jiang Q, Chopp M, Jahed M (2005) Introducing a new definition towards clinical detection of microvascular changes using diffusion and perfusion MRI. Sci Iranica 12:109–115
5. Ashoor M, Khorshidi A, Sarkhosh L (2019) Estimation of microvascular capillary physical parameters using MRI assuming a pseudo liquid drop as model of fluid exchange on the cellular level. Rep. Practical Oncol. Radiother. 24(1):3–11
6. Ashoor M, Khorshidi A, Pirouzi A, Abdollahi A, Mohsenzadeh M, Barzi SMZ (2021) Estimation of Reynolds number on microvasculature capillary bed using diffusion and perfusion MRI: the theoretical and experimental investigations. Eur. Phys. J. Plus 136:152
7. Ashoor M, Khorshidi A, (2016). Estimation of the number of compartments associated with the apparent diffusion coefficient in MRI: the theoretical and experimental investigations. AJR (Am. J. Roentgenol.) 206, 455–462
8. Goldman Maurice (2001) Advances in magnetic resonance formal theory of spin-lattice relaxation. J Magnetic Resonance 149:160–187
9. Yavuz E, Eyupoglu C (2020) An effective approach for breast cancer diagnosis based on routine blood analysis features. Med Biol Eng Comput 58:1583–1601. https://doi.org/10.1007/s11517-020-02187-9
10. Esslinger D, Rapp P, Knödler L, Preibsch H, Tarín C, Sawodny O, Brucker SY, Hahn M (2019) A novel finite element model–based navigation system–supported workflow for breast tumor excision. Med Biol Eng Comput 57:1537–1552. https://doi.org/10.1007/s11517-019-01977-0
11. Liu H, Wang J, Gao J, Liu S, Liu X, Zhao Z, Guo D, Dan G (2020) A comprehensive hierarchical classification based on multi-features of breast DCE-MRI for cancer diagnosis. Med Biol Eng Comput 58:2413–2425. https://doi.org/10.1007/s11517-020-02232-7
12. Zadeh Shirazi A, Seyyed Mahdavi Chabok SJ, Mohammadi Z. A novel and reliable computational intelligence system for breast cancer detection. Med Biol Eng Comput 2018; 56: 721–732. https://doi.org/10.1007/s11517-017-1721-z
13. Mustra M, Grgic M, Rangayyan RM (2016) Review of recent advances in segmentation of the breast boundary and the pectoral muscle in mammograms. Med Biol Eng Comput 54:1003–1024. https://doi.org/10.1007/s11517-015-1411-7
14. Ertas G, Doran SJ, Leach MO (2017) A computerized volumetric segmentation method applicable to multi-centre MRI data to support computer-aided breast tissue analysis, density assessment and lesion localization. Med Biol Eng Comput 55:57–68. https://doi.org/10.1007/s11517-016-1484-y
15. Yang SN, Li FJ, Liao YH, Chen YS, Shen WC, Huang TC (2015) Identification of breast cancer using integrated information from MRI and mammography. Plos one 10(6):e0128404. https://doi.org/10.1371/journal.pone.0128404

16. Ruiter NV, Stotzka R, Muller TO, Gemmeke H, Reichenbach JR, Kaiser WA (2006) Model-based registration of X-ray mammograms and MR images of the female breast. IEEE TRANSACTIONS ON NUCLEAR SCIENCE 53(1):204–211. https://doi.org/10.1109/TNS.2005.862983
17. Guo Y, Sivaramakrishna R, Lu CC, Suri JS, Laxminarayan S (2006) Breast image registration techniques: a survey. Med Bio Eng Comput 44:15–26. https://doi.org/10.1007/s11517-005-0016-y
18. Hu X, Jiang L, You C, Gu Y (2021) Fibroglandular tissue and background parenchymal enhancement on breast MR imaging correlates with breast cancer. Front. Oncol. 11:1–7. https://doi.org/10.3389/fonc.2021.616716
19. Omer M, Fear EC (2018) Automated 3D method for the construction of flexible and reconfigurable numerical breast models from MRI scans. Med Biol Eng Comput 56:1027–1040. https://doi.org/10.1007/s11517-017-1740-9
20. Zhou J, Li M, Liu D, Sheng F, Cai J (2023) Differential diagnosis of benign and malignant breast papillary neoplasms on MRI with non-mass enhancement. Acad Radiol 30:S127–S132
21. Dufaye G, Cherouat A, Bachmann JM (2013) Advanced modelling of the mechanical behaviour of biological tissues: application to 3D breast deformation. Comput Methods Biomech Biomed Engin 16(1):305–307
22. Pediconi F, Catalano C, Padula S, Roselli A, Dominelli V, Cagioli S, Kirchin MA, Pirovano G, Passariello R (2008) Contrast-Enhanced MR Mammography: improved lesion detection and differentiation with gadobenate dimeglumine. Ame J Roentgenol 191:1339–1346
23. Clauser P, Helbich TH, Kapetas P, Pinker K, Bernathova M, Woitek R, Kaneider A, Baltzer PAT (2019) Breast lesion detection and characterization with contrast-enhanced magnetic resonance imaging: prospective randomized intraindividual comparison of gadoterate meglumine (0.15 mmol/kg) and gadobenate dimeglumine (0.075 mmol/kg) at 3T. J Magn Reson Imaging 49(4):1157–1165
24. Kneeshaw PJ, Turnbull LW, Drew PJ (2003) Current applications and future direction of MR mammography. British J Cancer 88:4–10
25. Khorshidi A, Ashoor M, Abdollahi A (2023) Optimization of breast treatment planning towards lower dose rate: a Monte Carlo simulation study. Informatics in Medicine Unlocked 38:101220
26. Vourtsis A, Berg WA (2019) Breast density implications and supplemental screening. Eur Radiol 29(4):1762–77
27. Sprague BL, Stout NK, Schechter C et al (2015) Benefits, harms, and cost-effectiveness of supplemental ultrasonography screening for women with dense breasts. Ann Intern Med 162(3):157–66
28. Berg WAZZ, Lehrer D et al (2012) Detection of breast cancer with addition of annual screening ultrasound or a single screening MRI to mammography in women with elevated breast cancer risk. JAMA 307(13):1394–404
29. Gao Y, Reig B, Heacock L, Bennett DL, Heller SL, Moy L (2021) Magnetic resonance imaging in screening of breast cancer. Radiol Clin North Am. 59(1):85–98
30. Liu G, Xiao X, Song H, Kikkawa T (2021) Precise detection of early breast tumor using a novel EEMD-based feature extraction approach by UWB microwave. Med Biol Eng Comput 59:721–731. https://doi.org/10.1007/s11517-021-02339-5
31. Yin XX, Ng BWH, Ramamohanarao K, Gaghai-Wadji A, Abbott D (2012) Exploiting sparsity and low-rank structure for the recovery of multi-slice breast MRIs with reduced sampling error. Med Biol Eng Comput 50:991–1000. https://doi.org/10.1007/s11517-012-0920-x
32. Sage D, Unser M (2003) Teaching image-processing programming in Java. IEEE Signal Processing Magazine 20(6):43–52
33. Han SH, An YY, Kang BJ, Kim SH, Lee EJ (2016) Takeaways from pre-contrast T1 and T2 breast magnetic resonance imaging in women with recently diagnosed breast cancer. Iran J Radiol. 13(4):e36271
34. Khorshidi A, Ashoor M (2023) New deformity outline on the breast radiation therapy for diminishing absorbed dose ratio. Brazilian Journal of Radiation Sciences 11(3):1–12. https://doi.org/10.15392/2319-0612.2023.2281
35. Shahid H, Wiedenhoefer JF, Dornbluth C, Otto P, Kist KA (2016) An overview of breast MRI. J Appl Radiol 45: 7–13. Available online at: https://appliedradiology.com/articles/an-overview-of-breast-mri
36. Kuhl CK, Keulers A, Strobel K, Schneider H, Gaisa N, Schrading S (2018) Not all false positive diagnoses are equal: on the prognostic implications of false-positive diagnoses made in breast MRI versus in mammography/digital tomosynthesis screening. Breast Cancer Res 20:13. https://doi.org/10.1186/s13058-018-0937-7
37. Chu W, Jin W, Liu D, Wang J, Geng C, Chen L et al (2018) Diffusion-weighted imaging in identifying breast cancer pathological response to neoadjuvant chemotherapy: a meta-analysis. Oncotarget. 9:7088–7100. https://doi.org/10.18632/oncotarget.23195
38. Asgari A, Ashoor M, Sarkhosh L, Khorshidi A, Shokrani P (2019) Determination of gamma camera's calibration factors for quantitation of diagnostic radionuclides in simultaneous scattering and attenuation correction. Curr Radiopharm 12(1):29–39
39. Khorshidi A, Rajaee A, Ahmadinejad M, Ghoranneviss M, Ettelaee M (2014) Low energy electron generator design and depth dose prediction for micro-superficies tumor treatment purposes. Phys Scripta 89(9):095001–095006
40. Khorshidi A (2017) Accelerator driven neutron source design via beryllium target and 208Pb moderator for boron neutron capture therapy in alternative treatment strategy by Monte Carlo method. J Cancer Res Ther 13(3):456–465
41. Khorshidi A (2020) Accelerator-based methods in radio-material 99Mo/99mTc production alternatives by Monte Carlo method: the scientific-expedient considerations in nuclear medicine. J Multiscale Model 11(1):1930001
42. Colditz GA, Kaphingst KA, Hankinson SE, Rosner B (2012) Family history and risk of breast cancer: nurses' health study. Breast Cancer Res Treat. 133(3):1097–1104
43. Feng Y, Spezia M, Huang S, Yuan C, Zeng Z, Zhang L, Ji X, Liu W, Huang B, Luo W, Liu B, Lei Y, Du S, Vuppalapati A, Luu HH, Haydon RC, He TC, Ren G (2018) Breast cancer development and progression: Risk factors, cancer stem cells, signaling pathways, genomics, and molecular pathogenesis. Genes Dis. 5(2):77–106
44. King TA, Pilewskie M, Muhsen S et al (2015) A 29-year longitudinal experience evaluating clinicopathologic features and breast cancer risk. J Clin Oncol 33(33):3945–52
45. Saslow D, Boetes C, Burke W et al (2007) American Cancer Society guidelines for breast screening with MRI as an adjunct to mammography. CA Cancer J Clin 57(2):75–89
46. Riedl CC, Nikolaus L, Bernhart C et al (2015) Triple-modality screening trial for familial breast cancer underlines the importance of magnetic resonance imaging and questions the role of mammography and ultrasound regardless of patient mutation status, age, and breast density. J Clin Oncol 33(10):1128–35
47. Warner E, Messersmith H, Causer P et al (2008) Systematic review: using magnetic resonance imaging to screen women at high risk for breast cancer. Ann Intern Med 148(9):671–9
48. Evans DG, Harkness EF, Howell A et al (2016) Intensive breast screening in BRCA2 mutation carriers is associated with reduced breast cancer specific and all cause mortality. Heredit Cancer Clin Pract 14:8
49. Saadatmand S, Amarens Geuzinge H, Rutgers EJT et al (2019) MRI versus mammography for breast cancer screening in women with familial risk (FaMRIsc): a multicentre, randomised, controlled trial. Lancet Oncol 20(8):1136–47

50. Sung JS, Sarah S, Brooks J et al (2016) Breast cancer detected at screening MR imaging and mammography in patients at high risk: method of detection reflects tumor histopathologic results. Radiology 280(3):716–22
51. Bakker MF, de Lange SV, Pijnappel RM et al (2019) Supplemental MRI screening for women with extremely dense breast tissue. N Engl J Med 381(22):2091–102
52. Houssami N, Hunter K (2017) The epidemiology, radiology and biological characteristics of interval breast cancers in population mammography screening. NPJ Breast Cancer 3:12
53. Pataky R, Armstrong L, Chia S et al (2013) Cost-effectiveness of MRI for breast cancer screening in BRCA1/2 mutation carriers. BMC Cancer 13:339
54. Griebsch I, Broem J, Boggis C et al (2006) Cost-effectiveness of screening with contrast enhanced magnetic resonance imaging vs X-ray mammography of women at a high familial risk of breast cancer. Br J Cancer 95(7):801–10
55. Moore SG, Shenoy PJ, Fanucchi L et al (2009) Cost-effectiveness of MRI compared to mammography for breast cancer screening in a high risk population. BMC Health Serv Res 9:9
56. Mango VL, Goel A, Mema E et al (2019) Breast MRI screening for average-risk women: a Monte Carlo simulation cost-benefit analysis. J Magn Reson Imaging 49(7):e216-21
57. Birgani MT, Carloni V (2017) Tumor microenvironment, a paradigm in hepatocellular carcinoma progression and therapy. Int J Mol Sci 18(2):405

Mansour Ashoor The first author, Professor Mansour Ashoor, is an expert in health physics, nuclear imaging, MRI, and fuzzy mathematics who works at Nuclear Science and Technology Research Institute of Iran. He was responsible for checking the data from a health perspective and his advice during the project was very effective (https://www.researchgate.net/profile/Mansour-Ashoor).

Abdollah Khorshidi The second author, Dr. Abdallah Khorshidi, is an expert in medical radiation physics, nuclear medicine, and bioengineering. He conducted the study in such a way that he was the focus of all theoretical and practical preparations and even the writing and revising the article.